Mechanical Force Estimation Based on Visual Cell Deformation and Improved Point-Load Model

Yidi Zhang ⓘ, Yumeng Sun ⓘ, Shan Guo ⓘ, Maosheng Cui ⓘ, Xiangfei Zhao ⓘ, Qili Zhao ⓘ, *Member, IEEE*, Mingzhu Sun ⓘ, *Member, IEEE*, Xin Zhao ⓘ, *Member, IEEE*, and Yaowei Liu ⓘ, *Member, IEEE*

Abstract—Measuring the mechanical force applied to a cell during penetration has long been studied. However, existing sensor methods can disturb or even prevent a planned cell surgery because of their physical units. We propose a contactless mechanical force estimation method based on an improved point-load model and cell contour detection. We extended the point-load model to large cell deformations and obtained a relationship between the mechanical force and the morphology of the deformed cell. We designed two cell contour detection methods for visually detecting the deformation of different cell morphologies to obtain the geometric parameters required by the model. Finally, we carried out penetration experiments on porcine oocytes and zebrafish embryos. The contour detection methods showed a consistency of up to 99.29% compared with manual marking, and the force estimation accuracy was 1.05 μN. We compared the estimation results of our method with measurements taken in real experiments and confirmed that our method accurately estimated the mechanical force applied to the cell without contact. Thus, it may be applied to estimating the applied force during cell surgery in real time.

Index Terms—Cell detection, cell visual deformation, force analysis, mechanical force estimation, robotic cell manipulation.

I. INTRODUCTION

MICROMANIPULATION is the manipulation of cells or early embryos under a microscope with a micromanipulator and is widely used in bioengineering. One micromanipulation technique is microinjection or extraction, where a micropipette is used to penetrate a cell and deliver or draw materials. It is commonly applied in cell/embryo microinjection [1], [2], [3], [4], [5], [6], somatic cell nuclear transfer (SCNT) [7], [8], [9], and micro-dissection [10], [11]. Cell penetration is an essential step for microinjection or extraction, but this subjects the cell to the force applied by the micropipette, which can result in abnormal development or cell death [12], [13], [14], [15]. To minimize the cell damage, measuring the applied force during the penetration process is important. Many researchers have proposed techniques for measuring the applied force. Xu [16] designed a microelectromechanical systems (MEMS) microgripper with an integrated electrostatic actuator and capacitive force sensor to measure the applied force when an object is gripped. Sun et al. [17] proposed a polyvinylidene fluoride (PVDF) micro force sensor to detect the cell penetration force. Lu et al. [18] reported a piezoresistive force sensor that is fixed on the micropipette. Atomic force microscopy (AFM) is often employed in cantilever-based optical force measurements [19], [20], [21].

Although the above sensors accurately measure the applied force, some cannot be combined with micromanipulation systems. In addition, complex force sensors that are fixed to the micropipette can obstruct cell operations. Furthermore, contact measurements can cause additional cell damage. Therefore, the applied force to a cell needs to be measured without the installation of additional equipment. Sun et al. [22] proposed a point-load model to establish a quantitative relationship between the applied force and biomembrane structural deformation of cells. This approach is advantageous because the applied force can be calculated based on the morphology of the deformed cell. However, cell penetration usually causes significant deformation of the biomembrane, but the point-load model is only suitable for describing small deformations. Therefore, the point-load model needs to be expanded so that it can be applied to deformed cells.

We propose a mechanical force estimation method that combines visual detection of cell deformation with an improved point-load model. Penetration experiments using porcine oocytes (size: 100 μm) and zebrafish embryos (size: 1000 μm) were conducted to evaluate the performance of the proposed method. The rest of this article is organized as follows. Section II introduces the system setup and preparation process of the porcine oocytes and zebrafish embryos. Section III introduces the improved point-load model and two cell deformation detection methods tailored to the morphological characteristics of the porcine oocytes and zebrafish embryos.
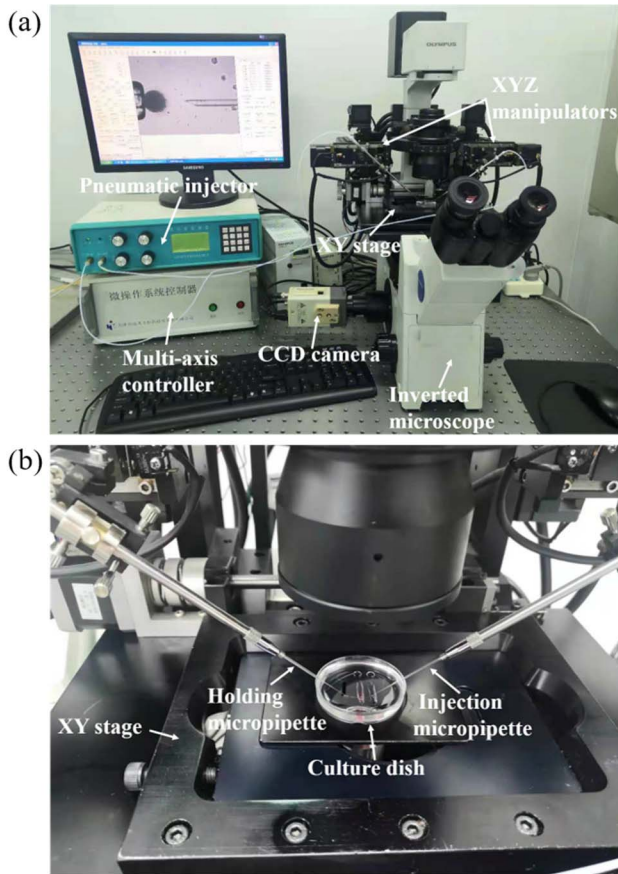
Fig. 1. Micromanipulation system for cell penetration experiments. (a) System setup. (b) Micro-operation workspace.

Section IV discusses the results of the two penetration experiments. Finally, Section V concludes the article.

II. SYSTEM OVERVIEW

A. System Setup

The cell penetration experiments were carried out on the self-developed NK-MR601 micro-operation system [23], [24], [25]. As shown in Fig. 1, the system is based on a standard inverted microscope (Olympus, BX-51, Japan). The platform is equipped with a self-developed electric two-degrees-of-freedom stage (*XY* stage) to position the culture dish containing cells. The stage has a travel range along the *XY* axis of 10 cm at a resolution of ± 0.1 μm and maximum speed of 2 mm/s. Two electric three-degrees-of-freedom operating manipulators (*XYZ* manipulators) hold the holding micropipette (HM) and injection micropipette (IM). The *XYZ* manipulators have a travel range of 50 mm along all three axes at a resolution of ± 0.1 μm and maximum speed of 1 mm/s. A self-developed pneumatic injector provides negative pressure (-3–0 kPa) and positive pressure (0–200 kPa). A self-developed multiaxis controller coordinates the movements of the stage and operating arm. A charge-coupled device (CCD) camera (W-V-460, Panasonic, Japan) captures images under the microscope at a frame rate of 20 fps and resolution of 768×576 pixels. A host is used to realize image processing, data acquisition, and motion control.

Oocyte operations took place under a $10\times$ objective lens with a spatial resolution of 0.625 μm, and embryo operations took place under a $4\times$ objective lens with a spatial resolution of 1.43 μm.

The HM was made from a borosilicate glass tube with an outer diameter of 1 mm and inner diameter of 0.6 mm. The glass tube was drawn by a micropipette puller (P-97, Sutter Instrument, USA) and was then forged into a microtube with a diameter of 50–80 μm by a forging needle instrument (MF-900, Narishige, Japan). Finally, the opening was melted by a professional with an alcohol lamp to make the needle smooth. The injection microneedle was purchased from CooperSurgical (TPC, LBC-OD20BA90, Australia). The tip had an outer diameter of 20 μm and tip angle of 45°.

B. Cell Preparation

Pig ovaries were taken from a slaughterhouse and were transported to the laboratory in a thermos flask filled with 35 °C–37 °C normal saline within 2 h. Then, the ovaries were immediately washed twice with 37 sterile saline containing 100 IU/L penicillin and 50 mg/L streptomycin. The oocytes were extracted from the 2–6 mm follicles on the ovary and were washed three times with TL-Hepes-PVA. The oocytes were then placed in an incubator at 39 °C and a CO_2 concentration of 5% for 42 h for in vitro maturation. The oocytes were taken out of the incubator and degloved with 0.1% hyaluronidase and were then washed three times with M199. The oocytes were then used directly in the penetration experiments.

1) Zebrafish Embryos: Freshly laid zebrafish eggs taken from the breeding facility were stored in room-temperature water for 4–6 h. They were then used in the penetration experiments.

III. MATERIALS AND METHODS

A. Force Estimation Based on Cell Deformation

When a micropipette touches the biomembrane, this produces a dimple with a tiny contact area between the cell and micropipette pinpoint at the center. This is considered the stress point of the cell. To obtain the applied force during the penetration process, the point-load model proposed by Sun et al. [22] was extended to large deformations of the biomembrane. In the model, the biomembrane is considered an elastomer that only deforms by stretching without obvious flexural rigidity. In addition, the membrane is assumed as subjected to hydrostatic pressure from the incompressible inner cytoplasm. Initially, no membrane stress and residual stress act on the cell, so the model represents the cell as a planar circle with zero residual stress.

When the cell is deformed by an applied force F from a micropipette with radius c, this creates a dimple with an inner radius c, outer radius a, and depth w_d around the stress points E_1 and E_2, as shown in Fig. 2. Projecting the dimple curve (from E_1 to $P_1 P_2$ and from E_2 to P_2) onto an unstressed plane perpendicular to the micropipette results in a circle with a small hole in the middle comprising many ring elements with a radius of r and width of dr. This is stretched to $dr/\cos$
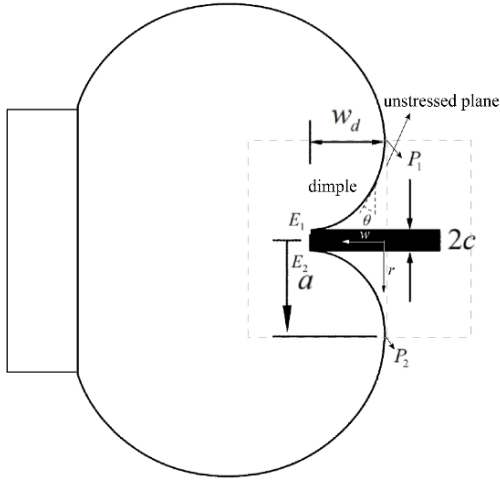
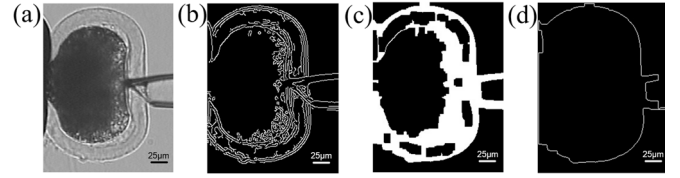Fig. 2. Deformation of a biomembrane by a micropipette.

Fig. 3. Oocyte deformation detection. (a) Live image of the deformed oocyte. (b) Canny edges. (c) Grayscale image after close operations. (d) Contour found and selected by adaptive area thresholding.

θ by the applied force, where θ is the angle between the unstressed plane and tangent plane at a point on the dimple of the membrane. During the penetration process, the applied force F is counterbalanced by the internal cell pressure and membrane stress σ_d and is expressed by

$$F = -\frac{4\pi w_d \sigma_d h}{\left[1 - (c/a)^2 + \ln(c/a)^2\right]} \quad (1)$$

where h is the membrane thickness. The values of w_d, a, h, and c are obtained from a real-time image of the deforming cell. σ_d is calculated by

$$\bar{\sigma}_d = \frac{E}{1 - v}\bar{\varepsilon}_d \quad (2)$$

where E represents Young's modulus of the membrane, v is Poisson's ratio, and ε_d is the average strain on the membrane. Within the dimple, every circle element of the membrane has a unique radius r and width dr. Because of the external load, every final circle element width is stretched to $dr/\cos\theta$. Thus, the elastic strain ε_d on each circle element is given by

$$\varepsilon_d = \frac{\frac{dr}{\cos\theta} - dr}{dr} = \sec\theta - 1. \quad (3)$$

In the preexisting point-load model, the largest θ was assumed as less than 22° for small angle and strain approximations. However, the small strain approximation is invalid for the cell penetration process because of the large θ caused by the obvious membrane deformation. Previous research [26], [27] has shown that the half-planar dimple curve of a deformed zebrafish embryo caused by a micropipette can be fit to a parabola. Thus, the shape of the planar membrane dimple $E_1 P_1(E_2 P_2)$ can be described by a parabolic model, where the relationship between the depth w and radius r is given by

$$w \approx -\frac{w_d}{(a - c)^2}(a - r)^2 + w_d. \quad (4)$$

The angle θ between the tangent plane at a point on the membrane dimple and unstressed plane can be obtained by

$$\theta = \arctan\frac{2w_d(a - r)}{(a - c)^2}. \quad (5)$$

Because the elastic strain of the membrane can be calculated from the change in membrane area and a negligible second-order term, the average strain on the membrane is given by

$$\begin{aligned}\bar{\varepsilon}_d &= \frac{1}{2}\frac{\int_c^a (\sec\theta - 1)r\,dr}{\int_c^a r\,dr} \\ &= \frac{a\sqrt{1 + t^2} - 2a}{2(a + c)} + \frac{a\ln\left(t + \sqrt{1 + t^2}\right) + 2w_d}{2t(a + c)} \\ &\quad + \frac{2w_d - 2w_d\left(1 + t^2\right)^{\frac{3}{2}}}{3t^3(a + c)}\end{aligned} \quad (6)$$

where

$$t = \tan\theta_d = \frac{2w_d}{a - c}. \quad (7)$$

The membrane stretching stress σ_d can be acquired by combining (2) and (7). Then, the force applied by the micropipette can be estimated by using (1) after acquisition of four geometric parameters: w_d, h, c, and a.

B. Cell Deformation Detection and Parameter Acquisition

As given in (1), five parameters are needed to estimate the applied force. h and c are constants that can be detected manually before cell penetration. As the micropipette penetrates toward the center of the cell horizontally, the resulting dimple becomes wider and deeper, and the outer radius a and depth w_d change accordingly. As shown in Fig. 1, a and w_d can be acquired from the position difference between the dimple top $E_1(E_2)$ and dimple base $P_1(P_2)$, which can be identified and marked as feature points by deformation detection. The membrane stress σ_d can be calculated from a, c, and w_d by using (2)–(7). Thus, we developed two cell deformation detection methods tailored to the morphological characteristics of porcine oocytes and zebrafish embryos to identify feature points.

1) Oocyte Deformation Detection: As shown in Fig. 3(a), the zona pellucida (ZP) of oocytes is almost transparent with a pixel value close to that of the internal cytoplasm, perivitelline space, and dish environment. Thus, we employed a contour detection method suitable for cases with unclear contours. Algorithm 1 shows the detection procedure, and Fig. 3 shows the intermediate steps. First, the source color images of the oocyte shown in Fig. 3(a) are converted into grayscale images. Second, the grayscale images are blurred by the OpenCV function blur to reduce image noise. Third, the OpenCV function Canny is employed to find the object edges. This function performs well at eliminating fake edges

Algorithm 1 Contour Detection Algorithm

1: **procedure** CELLCONTOURDETECTION(I, *threshold*)
2:    $I_{gray} \leftarrow$ cvtColor(I)
3:    $\bar{I}_{gray} \leftarrow$ blur(I_{gray})
4:    $I_c \leftarrow$ Canny($\bar{I}_{gray}$)
5:    $I_c' \leftarrow$ morphologyEx(I_c, cv::MORPH_CLOSE)
6:    $Seq_i \leftarrow$ findContours(I_c')
7:   **if**   contourArea(Seq_i) > *threshold*
8:      $Seq \leftarrow Seq_i$
9:   **end**
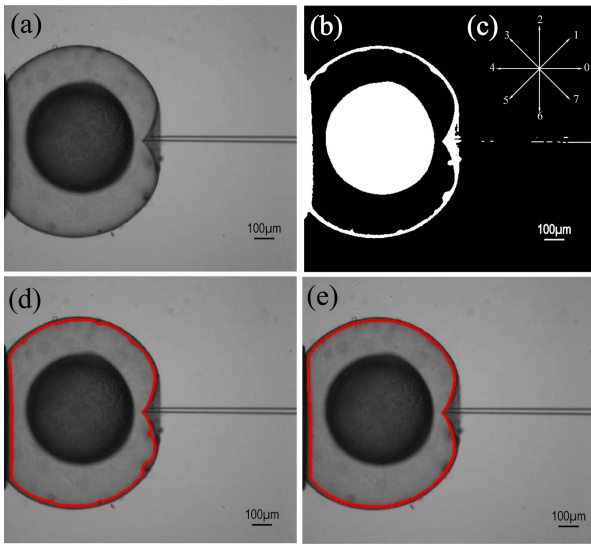10: **return** Seq
11: **end procedure**

Fig. 4. Zebrafish embryo deformation detection. (a) Live image of the deformed zebrafish embryo. (b) Binary live image after initial adaptive thresholding. (c) Definition of the direction variable dir. (d) Inner contour detected. (e) Inner contour smoothed.

by setting two artificial thresholds to identify the strong and weak edges. The result is shown in Fig. 3(b). Fourth, because of the slender ZP contour, there are many useless edges inside the cell area after the Canny edge detection. Thus, the resulting images are closed morphologically to emphasize the strong ZP edge and hide the negligible inner edges, as shown in Fig. 3(c). Fifth, the oocyte contours are identified by the OpenCV function findContours and are selected by setting an appropriate contour area threshold. The final detected contour of the deformed cell is shown in Fig. 3(d).

2) Zebrafish Embryo Deformation Detection: Fig. 4(a) shows that the ZP of the zebrafish embryos has a clear inner contour with a clean space beneath it. Thus, it is more convenient to extract the geometric parameters of the deformed cells by detecting the inner contour of the embryo. We developed a detection algorithm for extracting the inner contour of the zebrafish embryos based on distribution rules for pixel values in the binary image.

1) A median filter is used to denoise the source color images.

2) The filtered images are converted to grayscale images.
3) The grayscale images are processed into binary images [see Fig. 4(b)].
4) The binary images are traversed from left to right and from top to bottom, until the first non-zero pixel is found. This is defined as the upper peak of the outer embryo contour. Then, the first zero pixel is found vertically downward, and the non-zero point above it is taken as the beginning of the detected contour P_0, which is defined as the upper peak of the inner embryo contour.
5) Before the contour is searched, a direction variable dir with an initial value of zero is set to store the direction of the current pixel position relative to the last one. This is employed to identify the starting direction of the next contour point search. There are eight available directions corresponding to the eight pixels around the current position, which are numbered from 0 to 7 anticlockwise from the right [see Fig. 4(c)].
6) The starting direction to search for the next contour point is identified based on dir. If dir is even, then the starting direction is (dir + 7) mod8. If dir is odd, then the starting direction is (dir + 6) mod8.
7) The new contour point P_n is found, which is the first non-zero pixel visited clockwise from the identified starting direction. A set of contour points $(P_0, \ldots, P_n)$ are found as the inner contour of the embryo by repeating step 6 until $P_n = P_1$ and $P_{n-1} = P_0$ [see Fig. 4(d)].

As shown in Fig. 4(d), the detected contour is not smooth enough to describe the cell contour accurately because of impurities adhering to the membrane. Based on the convexity of the cell contour, we propose the following contour smoothing algorithm. For any point P_i on the embryo contour, there are points P_{i-5} and P_{i+5} in the contour sequence and a point P_c inside the embryo contour. When P_i and P_c are on different sides of the connection between P_{i-5} and P_{i+5}, we can assume that the segment with P_i is smooth. When P_i and P_c are on the same side of the connection between P_{i-5} and P_{i+5}, P_i needs to move along the perpendicular direction of the connection between P_{i-5} and P_{i+5} until P_i and P_c are on different sides. Then, the next pixel point is considered and so on until all points on the contour have been considered. To achieve a better smoothing effect, the above steps should be repeated three times [see Fig. 4(e)].

3) Feature Point Identification and Parameter Acquisition: The detected cell contours can then be used to determine the positions of feature points according to the morphological characteristics of the two dimple bases P_1 and P_2 on the deformed cell and the cell load point (E_1 or E_2).

a) Oocyte feature point identification: In the set of detected oocyte contours, we consider the point with the largest horizontal coordinate on the upper or lower side of the micropipette as a dimple base. We usually remove the area of the micropipette to ensure that it no longer interferes with the selection of dimple bases. Considering the half contour on the upper side of the micropipette, if both P_{i-3} and P_{i+3} of the set of contours are on the left side of P_i, then P_i can
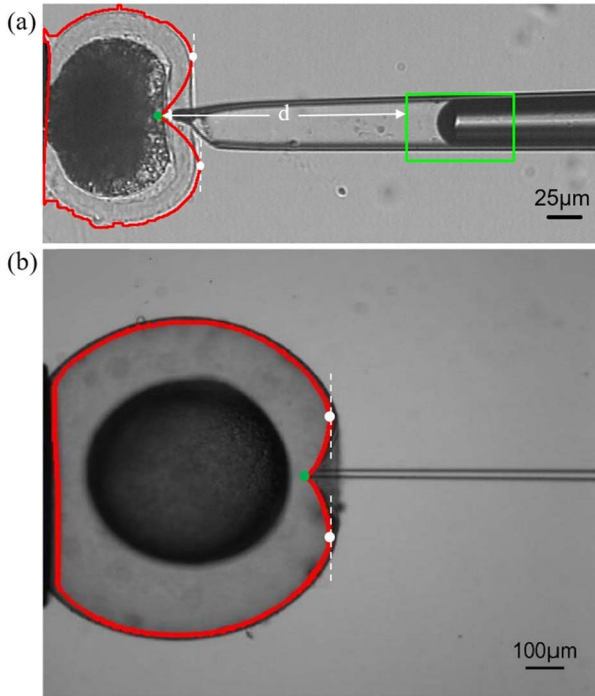
Fig. 5. Identification of feature points based on detected contours. (a) Micropipette pinpoint detected by template matching method, and two dimple bases identified based on the morphological characteristics of the contours. Green rectangle: template; green point: micropipette pinpoint; white point: dimple base. (b) Cell load point and two dimple bases detected based on the morphological characteristics of contours. Green point: cell load point; white point: dimple base.

be regarded as the upper dimple base P_1. P_2 can be found similarly, as shown by the white spots in Fig. 5(a).

In the set of detected oocyte contours, we consider the point with the smallest horizontal coordinate in the dimple part of the detected contour as the cell load point. However, as shown in Fig. 2(a), the load point of the oocyte ZP is difficult to identify because of the low transparency of the cytoplasm. Fortunately, we observed that the cell load point and pinpoint coincide, which was verified experimentally (see Appendix A). However, the pinpoint is difficult to observe because the tip is hidden in the dimple after the micropipette touches the biomembrane. The micropipette is a rigid body, so the distance between any two parts of it is constant. We can extract the part of the micropipette containing the gas–liquid interface as a template and measure the distance d between the pinpoint and template. Then, we can update the template position by the template matching method, and the pinpoint is at a distance d from the template. Then, the detected position of the pinpoint can be regarded as the cell load point, as shown by the green spot in Fig. 5(a).

b) Zebrafish embryo feature point identification: Similarly, we can consider the point in the set of detected contours of the zebrafish embryo with the largest horizontal coordinate on the upper or lower side of the micropipette as a dimple base. For the half contour on the upper side of the micropipette, if both P_{i-3} and P_{i+3} of the contour set are on the left side of P_i, then P_i can be regarded as the upper dimple base P_1. P_2 can be found similarly, as shown by the white spots

in Fig. 5(b). We can consider the point with the smallest horizontal coordinate in the dimple part of the detected contour as the cell load point. Because the inner contours of the zebrafish embryo are clear enough to detect, the cell load point can be easily identified. If both P_{i-3} and P_{i+3} of the inner contour are on the right side of P_i, then P_i can be regarded as the cell load point, as shown by the green spot in Fig. 5(b).

c) Parameter acquisition: Finally, the horizontal and perpendicular distances w_d and a between the deepest point of the dimple and the right-hand side summit of the deformed membrane are, respectively, given by

$$a = \frac{y_{P_2} - y_{P_1}}{2} \tag{8}$$

$$w_d = \max\left(x_{P_1} - x_{E_1}, x_{P_2} - x_{E_2}\right). \tag{9}$$

IV. RESULTS

A. Cell Deformation Detection

We applied Algorithm 1 to detect porcine oocyte deformation and Algorithm 2 to detect zebrafish embryo deformation during the penetration process. Ten oocytes and ten zebrafish embryos were employed for the penetration experiments (Supplementary Videos S1 and S2).

1) Oocyte Contour Detection: Before contact between the micropipette and cell, the ZP edge of the oocyte could be detected almost completely and accurately. When the micropipette touched the oocyte and caused a dimple, the pinpoint of the micropipette and contour of dimple were mostly hidden because of the low transparency of the oocyte cytoplasm and high transparency of the ZP. With Algorithm 1, the feature points of the deformed oocyte were obtained. The two right summits of the membrane (dimple bases P_1 and P_2) were obtained from the detected contour because they were not obscured by the cytoplasm. The pinpoint position of the micro-pipette was identified by the template matching method. The contour of the obscured part was fit to a parabola by using (4), based on the acquired outer radius a and depth w_d of the dimple. Fig. 6 shows the contour of the oocyte during the penetration process; the contour is marked with a red curve, the dimple bases are marked by white spots, and the cell load point is marked by a green spot. Video S1 gives the detection results. To evaluate the performance of the contour detection method, we manually labeled the cell contours and calculated the consistency

$$\text{Consistency} = 1 - \frac{(\text{RA} - \text{CA})}{\text{RA}} \tag{10}$$

where RA is the real area of the planar cell as determined by the manual labeling and CA is the area of detected contour. The consistency was found to be 97.91%.

2) Zebrafish Embryo Contour Detection: We used Algorithm 2 to detect and smooth the inner contours of the deformed zebrafish embryos during the penetration process. The real-time images of the results are shown in Fig. 7, where the dimple bases are marked by white spots and the cell load point is marked by a green spot. Video S2 gives the detection results. We used (10) to calculate the consistency
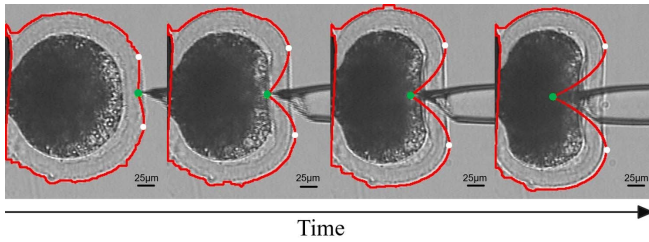
Fig. 6. Detection of oocyte deformation contours and feature points in penetration experiments. The horizontal axis "time" indicates that the images are arranged in chronological order.
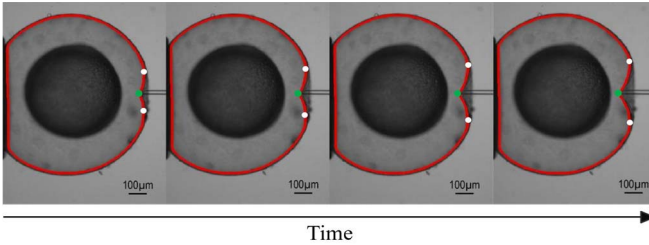

Fig. 7. Detection of zebrafish embryo deformation contours and feature points in penetration experiments. The horizontal axis "time" indicates that the images are arranged in chronological order.

between the detected contours and manual labeling results and found that the consistency was 99.29%.

B. Mechanical Force Estimation

1) Oocyte: We used the detected contours of the continuously deformed porcine oocytes in the improved point-load model to estimate the penetration force. We assumed that the ZP and cytoplasm are incompressible and that the volume remained unchanged when deformed. Thus, we set Poisson's ratio v to 0.5. The Young's modulus E of the ZP was 20 kPa, the thickness h of the ZP was 20 μm, and the radius c of the contact area between the pinpoint and membrane was 3 μm (see the Appendix for more details). Figs. 6 and 8 show the results for the deformation detection and penetration force estimation. The penetration force increased with the penetration depth, and the penetration force was estimated with a precision of 1.05 μN on average.

2) Zebrafish Embryo: The mechanical force was also estimated in three zebrafish embryo penetration experiments. The detected contours were used to estimate the applied force according to (1). Based on the incompressibility of the embryos, Poisson's ratio v was set to 0.5. The Young's modulus E was set to 1.5 MPa, and the thickness h of the ZP and radius c of the micropipette pinpoint were both set to 10 μm (see the Appendix for more details). Figs. 7 and 9 show the results for the deformation detection and penetration force estimation. The penetration force was estimated with a precision of 27 μN on average.

C. Verification

We measured the mechanical force applied on the zebrafish embryo by the force sensor (VK-701H, Weijingyi Electronics (Shenzhen) Company, Ltd., China) and compared the model estimation results of zebrafish embryos with our measurement
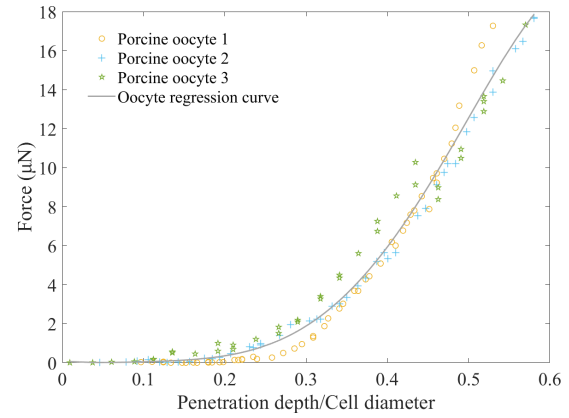

Fig. 8. Modeling results of porcine oocytes during the penetration experiments with the improved point-load model.
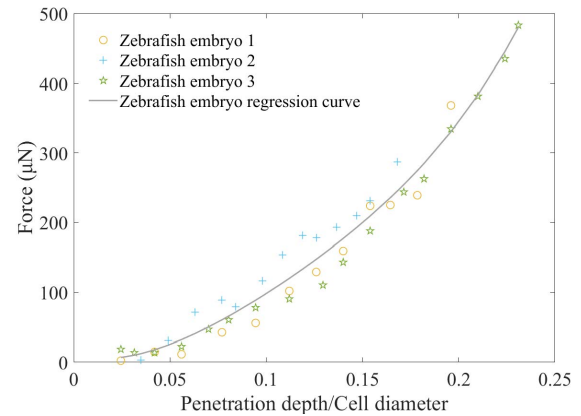

Fig. 9. Modeling results of zebrafish embryos during the penetration experiments with the improved point-load model.
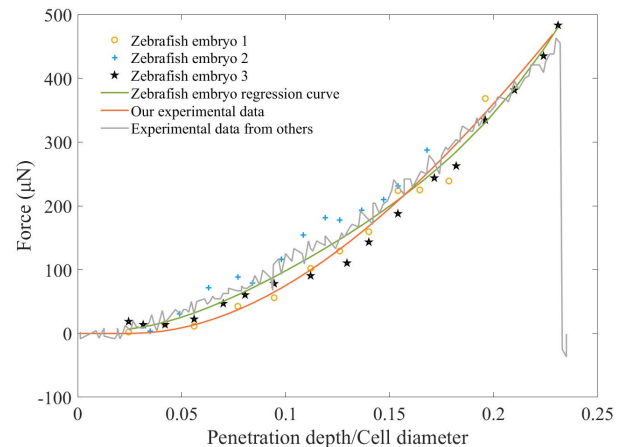
Fig. 10. Comparison between the experimental data and modeling results of zebrafish embryos during the penetration experiments.

results and experimental data of Xie et al. [28]. As shown in Fig. 10, our estimation results had the same trend and magnitude as the experimental results. The coefficient of determination R^2 of our improved model was 97.81%. Compared with the experimental measurement results, the average error of the model estimation results is 11.34 μN, which is less than 3.23% of the maximum force (puncture force). Considering
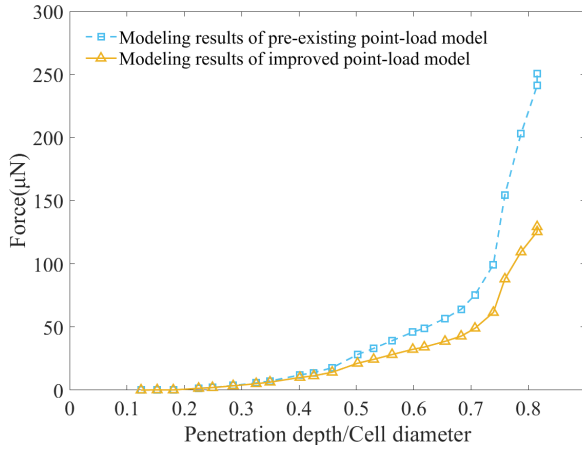
Fig. 11. Comparison between the modeling results of porcine oocytes during the penetration experiments with the preexisting and improved point-load models.
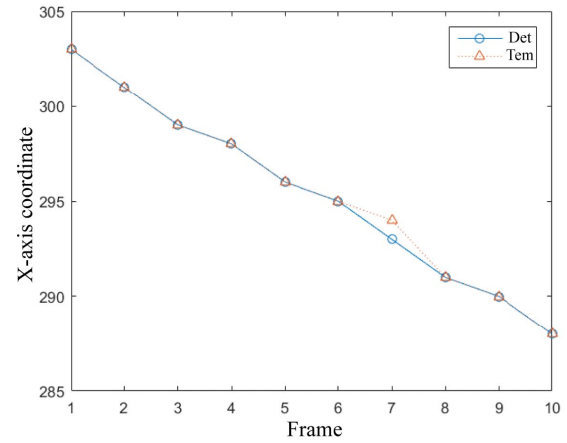

Fig. 12. Positions of the cell load point identified from the detected cell contours and micropipette pinpoint identified by the template matching method.

the differences between individual zebrafish embryos, the measurement accuracy was satisfactory.

To verify that our method could accurately estimate the force on a cell with a large deformation, we compared its performance with that of the preexisting point-load model proposed by Sun et al. [22] using the same batch of zebrafish embryos. As shown in Fig. 11, for slight deformations (i.e., penetration depth of less than 0.4 times the diameter of the oocyte), the average relative error between the two methods was 6.27%. As the penetration depth increased, the results of the two methods increasingly diverged, and the average relative error became 51.24%. When the penetration depth reached 0.8 times the oocyte diameter, the force estimated by the preexisting point-load model was almost twice that of the improved model. The angle approximations applied by the preexisting model were not suitable for the large deformations of the porcine oocytes during the penetration process. These results are consistent with the analysis in Section III-A.

V. CONCLUSION

We propose a contactless method based on an improved point-load model to estimate the applied force on a cell during micropipette penetration. We extended the point-load model proposed by Sun et al. to account for the large deformation that a cell may undergo before being punctured. We developed two algorithms for detecting and smoothing the contours of oocytes and zebrafish embryos, which can then be used to extract the geometric parameters required for mechanical force estimation. We performed penetration experiments on porcine oocytes and zebrafish embryos, and the proposed method demonstrated highly accurate contour detection and very sensitive mechanical force estimation. The estimation results obtained by the proposed method were consistent with experimental data, and the model more accurately estimated the applied force on cells with large deformations than the preexisting point-load model. The contactless mechanical force estimation method does not eliminate the need for physical devices but can be used to estimate and control the forces applied by micromanipulators used in cell surgery to minimize

cell damage. The proposed method has great potential for applications in cell physiology and pathology.

APPENDIX

A. Position Comparison of the Cell Load Point and Micropipette Pinpoint

Here, we validate the assumption that the cell load point and micropipette pinpoint coincide, which would allow the cell load point to be inferred from the detected pinpoint position. However, the micropipette pinpoint is covered by the oocyte like the dimple top. To acquire the pinpoint position, we first extracted the part of the micropipette containing the gas–liquid interface as a template and measured the distance d between the pinpoint and template. Subsequently, we updated the template position by the template matching method so that the pinpoint can be inferred to be at a distance d from the template.

We used the standard square deviation matching method for template matching. The correlation coefficient is given by

$$R(x, y) = \frac{\sum_{x',y'} \left(T\left(x', y'\right) - I\left(x + x', y + y'\right)\right)^2}{\sqrt{\sum_{x',y'} T(x', y')^2 \sum_{x',y'} I(x + x', y + y')^2}} \quad \text{(A1)}$$

where $T(x', y')$ is the pixel value of the point (x', y') on the template image and $I(x + x', y + y')$ is the pixel value of the corresponding position on the image to be matched. The position with the lowest correlation coefficient is the updated template position.

If we take the zebrafish embryo as an example, we can compare the x-axis coordinate of the cell load point based on the detected inner contour with the x-axis coordinate of the micropipette pinpoint obtained by template matching. As shown in Fig. 12, among the ten detected frames, only one pair of frames has an error of one pixel, and the other pairs are consistent with the assumption. These results validate the assumption that the cell load point and micropipette pinpoint coincide.

B. Measurement of ZP Young's Modulus

We estimated Young's modulus of the ZP by using the widely used shell model, which assumes that the cell is
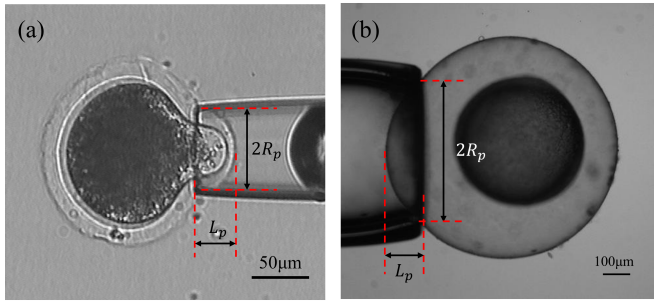
Fig. 13. Measurement of Young's modulus of the ZP. (a) Oocyte. (b) Zebrafish embryo.
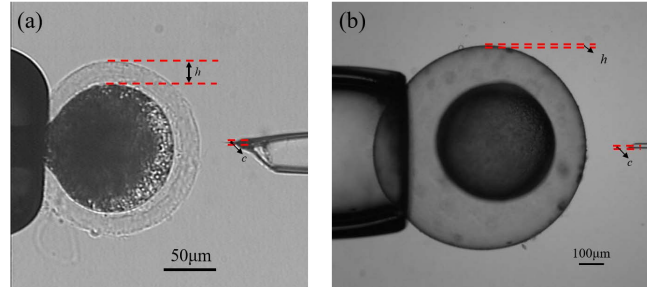

Fig. 14. Measuring ZP's thickness and micropipette pinpoint radius. (a) Oocyte experiments. (b) Zebrafish embryo experiments.

compressible, homogeneous, and covered by an elastic layer of finite thickness on an isotropic elastic cytoplasm [29], [30], [31]. The model is expressed by

$$E = 2C(h^*)(1 - v^2)\left(\frac{\Delta P}{\Delta L/R_p}\right) \quad (A2)$$

where h^* is the dimensionless thickness of the oocyte, which is defined as the ratio of the thickness of the ZP (h) to the radius of the micropipette (R_p). $C(h^*)$ is a function of h^*, and v is Poisson's ratio. We set $v = 0.5$ assuming that the ZP and cytoplasm are incompressible and that the volume remains constant during deformation. The Young's modulus was measured in a micropipette aspiration experiment during which the suction pressure ΔP, increment with the changing of the aspiration pressure ΔL, and micropipette radius R_p could be obtained, as shown in Fig. 13. Based on (A2), Young's modulus of the oocyte ZP was measured as 19.8 ± 1.6 kPa ($n = 15$). Similarly, we obtained Young's modulus of zebrafish ZP as 1.50 ± 0.13 MPa ($n = 15$).

C. Measurement of ZP Thickness and Micropipette Pinpoint Radius

The thickness of the ZP of the oocytes was obtained by microscopy image processing. We calculated the ZP thickness and pinpoint radius by counting the pixels occupied by the ZP and the ratio of the pixels to the actual size. Fig. 14(a) shows the image when the oocyte ZP thickness was 20 μm and the micropipette pinpoint radius was 3.0 μm. Fig. 14(b) shows the figures when the zebrafish embryo ZP thickness was 10 μm and the micropipette pinpoint radius was 10 μm.

ACKNOWLEDGMENT

REFERENCES

[1] M. Ammi and A. Ferreira, "Realistic visual and haptic rendering for biological-cell injection," in *Proc. IEEE Int. Conf. Robot. Autom.*, Apr. 2005, pp. 918–923.

[2] A. M. Tabbalat, N. Pereira, D. Klauck, C. Melhem, R. T. Elias, and Z. Rosenwaks, "Arabian peninsula ethnicity is associated with lower ovarian reserve and ovarian response in women undergoing fresh ICSI cycles," *J. Assist. Reproduction Genet.*, vol. 35, no. 2, pp. 331–337, Feb. 2018.

[3] Z. Lu, X. Zhang, C. Leung, N. Esfandiari, R. F. Casper, and Y. Sun, "Robotic ICSI (intracytoplasmic sperm injection)," *IEEE Trans. Biomed. Eng.*, vol. 58, no. 7, pp. 2102–2108, Jul. 2011.

[4] J. Park, S.-H. Jung, Y.-H. Kim, B. Kim, S.-K. Lee, and J.-O. Park, "Design and fabrication of an integrated cell processor for single embryo cell manipulation," *Lab Chip*, vol. 5, no. 1, p. 91, 2005.

[5] P. Stein and R. M. Schultz, "ICSI in the mouse," *Methods Enzymology*, vol. 476, no. 10, pp. 251–262, 2010.

[6] W. Wang, X. Liu, D. Gelinas, B. Ciruna, and Y. Sun, "A fully automated robotic system for microinjection of zebrafish embryos," *PLoS ONE*, vol. 2, no. 9, p. e862, Sep. 2007.

[7] A. G. Curcio, F. F. Bressan, F. V. Meirelles, and A. J. B. Dias, "Achievements and perspectives in cloned and transgenic cattle production by nuclear transfer: Influence of cell type, epigenetic status and new technology," *Animal Reproduction*, vol. 14, no. 4, pp. 1003–1013, 2017.

[8] A. Dinnyés, P. De Sousa, T. King, and I. Wilmut, "Somatic cell nuclear transfer: Recent progress and challenges," *Cloning Stem Cells*, vol. 4, no. 1, pp. 81–90, Mar. 2002.

[9] Z. Liu et al., "Cloning of macaque monkeys by somatic cell nuclear transfer," *Cell*, vol. 172, no. 4, pp. 881–887, Feb. 2018.

[10] L. G. Chen, Y. X. Liu, and L. N. Sun, "Piezo-powered micro-dissection system with ultrasonic vibration," in *Proc. 30th Chin. Control Conf. (Ccc)*, 2011, pp. 6067–6071.

[11] P. C. King, S. H. Zahiri, and M. Jahedi, "Focused ion beam microdissection of cold-sprayed particles," *Acta Mater.*, vol. 56, no. 19, pp. 5617–5626, Nov. 2008.

[12] C. V. C. Bouten, R. G. M. Breuls, E. A. G. Peeters, C. W. J. Oomens, and F. P. T. Baaijens, "In vitro models to study compressive strain-induced muscle cell damage," *Biorheology*, vol. 40, nos. 1–3, pp. 383–388, 2003.

[13] C. V. C. Bouten, M. M. Knight, D. A. Lee, and D. L. Bader, "Compressive deformation and damage of muscle cell subpopulations in a model system," *Ann. Biomed. Eng.*, vol. 29, no. 2, pp. 153–163, Feb. 2001.

[14] F. Liu, D. Wu, X. Wu, and K. Chen, "Analyses of the cell mechanical damage during microinjection," *Soft Matter*, vol. 11, no. 7, pp. 1434–1442, 2015.

[15] A. Scott, K. M. Khan, J. Heer, J. L. Cook, O. Lian, and V. Duronio, "High strain mechanical loading rapidly induces tendon apoptosis: An ex vivo rat tibialis anterior model," *Brit. J. Sports Med.*, vol. 39, no. 5, p. e25, May 2005.

[16] Q. Xu, "Design, fabrication, and testing of an MEMS microgripper with dual-axis force sensor," *IEEE Sensors J.*, vol. 15, no. 10, pp. 6017–6026, Oct. 2015.

[17] Z. Sun, L. Hao, W. Chen, and Z. Li, "Robotic cell injection force control based on static PVDF sensor and fuzzy-PID control method," *Int. J. Appl. Electromagn. Mech.*, vol. 41, no. 1, pp. 73–86, 2013.

[18] Z. Lu, P. C. Y. Chen, J. Nam, R. Ge, and W. Lin, "A micromanipulation system with dynamic force-feedback for automatic batch microinjection," *J. Micromech. Microeng.*, vol. 17, no. 2, pp. 314–321, 2007.

[19] J. Liu, J. Wen, Z. Zhang, H. Liu, and Y. Sun, "Voyage inside the cell: Microsystems and nanoengineering for intracellular measurement and manipulation," *Microsystems Nanoengineering*, vol. 1, no. 1, Dec. 2015, Art. no. 15020.

[20] X. Meng, X. Wu, J. Song, H. Zhang, M. Chen, and H. Xie, "Quantification of the microrheology of living cells using multi-frequency magnetic force modulation atomic force microscopy," *IEEE Trans. Instrum. Meas.*, vol. 71, pp. 1–9, 2022.

[21] X. Zhu, X. Liu, and Z. Wang, "Measurement of viscoelastic properties of living SMCC-7721 cells by atomic force microscopy," in *Proc. IEEE Int. Conf. Manipulation, Manuf. Meas. Nanoscale (M-NANO)*, Jul. 2016, pp. 155–158.

[22] Y. Sun, K. T. Wan, K. P. Roberts, J. C. Bischof, and B. J. Nelson, "Mechanical property characterization of mouse zona pellucida," *IEEE Trans. Nanobiosci.*, vol. 2, no. 4, pp. 279–286, Dec. 2003.

[23] N. Li et al., "High-precision, pressure-driven pump for sub-picoliter scale quantitative injection," *Modern Phys. Lett. B*, vol. 31, no. 13, May 2017, Art. no. 1750148.

[24] Y. Liu, M. Cui, J. Huang, M. Sun, X. Zhao, and Q. Zhao, "Robotic micropipette aspiration for multiple cells," *Micromachines*, vol. 10, no. 5, p. 348, May 2019.

[25] H. Gong et al., "Automatic cell rotation based on real-time detection and tracking," *IEEE Robot. Autom. Lett.*, vol. 6, no. 4, pp. 7909–7916, Oct. 2021.

[26] M. L. Han, Y. L. Zhang, C. Y. Shee, and W. T. Ang, "Vision based cell strain modeling and control system," in *Proc. 3rd IEEE RAS EMBS Int. Conf. Biomed. Robot. Biomechatronics*, Sep. 2010, pp. 698–703.

[27] Z. Lu, P. C. Y. Chen, H. Luo, J. Nam, R. Ge, and W. Lin, "Models of maximum stress and strain of zebrafish embryos under indentation," *J. Biomechanics*, vol. 42, no. 5, pp. 620–625, Mar. 2009.

[28] Y. Xie, D. Sun, C. Liu, H. Y. Tse, and S. H. Cheng, "A force control approach to a robot-assisted cell microinjection system," *Int. J. Robot. Res.*, vol. 29, no. 9, pp. 1222–1232, 2010.

[29] L. G. Alexopoulos, M. A. Haider, T. P. Vail, and F. Guilak, "Alterations in the mechanical properties of the human chondrocyte pericellular matrix with osteoarthritis," *J. Biomechanical Eng.*, vol. 125, no. 3, pp. 323–333, 2003.

[30] M. Khalilian, M. Navidbakhsh, M. R. Valojerdi, M. Chizari, and P. E. Yazdi, "Estimating Young's modulus of zona pellucida by micropipette aspiration in combination with theoretical models of ovum," *J. Roy. Soc. Interface*, vol. 7, no. 45, pp. 687–694, Apr. 2010.

[31] Q. Zhao et al., "A novel pneumatic micropipette aspiration method using a balance pressure model," *Rev. Sci. Instrum.*, vol. 84, no. 12, 2013, Art. no. 123703.

Xiangfei Zhao received the B.S. degree from the Department of Wind Energy and Power Engineering, Hebei University of Technology, Tianjin, China, in 2013, and the M.A. degree from the Automation College of Tianjin University of Technology, Tianjin, in 2017. He is currently pursuing the Ph.D. degree in control theory and control engineering with Nankai University, Tianjin.

His current research interests include micromanipulators and micro- and nanorobotics.

Yidi Zhang was born in 1997. She received the bachelor's degree in automation from the Hebei University of Technology, Tianjin, China, in 2019. She is currently pursuing the Ph.D. degree with the School of Artificial Intelligence, Nankai University, Tianjin.

Her current research interests include micromanipulation and micro- and nanorobotics.

Yumeng Sun was born in 1995. She received the bachelor's degree in automation and master's degree in control science and engineering from Nankai University, Tianjin, China, 2017 and 2020, respectively.

Her graduate studies were mostly focused on the deformation and stress of cells based on computer vision.

Shan Guo was born in 1989. He received the Ph.D. degree in control science and engineering from Nankai University, Tianjin, China, in 2021.
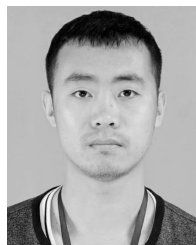
He is now a Post-Doctoral Fellow at the College of Artificial Intelligence, Nankai University. He is also with the Institute of Intelligence Technology and Robotic Systems, Shenzhen Research Institute of Nankai University, Shenzhen, China. His current research interests include modeling and simulation of biological systems and chemical computing.

Maosheng Cui received the B.A. degree from the Department of Animal Science, Anhui Technologic College, Hefei, China, in 2003, the M.A. degree from the Animal Science College, Yunnan Agricultural University, Kunming, Yunnan, China, in 2006, and the Ph.D. degree from the Animal Science College, Chinese Agricultural University, Beijing, China, in 2009.

He was a Post-Doctoral Researcher with the Chinese Academy of Agricultural Sciences from 2011 to 2013. He is with the Institute of Intelligence Technology and Robotic Systems, Shenzhen Research Institute of Nankai University, Shenzhen, China. He is also working at the Tianjin Animal Sciences Institute, Tianjin, China, as an Associate Investigator in the study and application of reproduction biotechnology in domestic animals.

Qili Zhao (Member, IEEE) received the B.Eng. degree in automation from the Shandong University of Science and Technology, Qingdao, China, in 2008, and the Ph.D. degree in control theory and control engineering from Nankai University, Tianjin, China, in 2014.

He finished his first Post-Doctoral Research with the Robotics and Mechatronics Research Laboratory, Department of Mechanical and Aerospace Engineering, Monash University, Melbourne, VIC, Australia, in 2015. He was a Post-Doctoral Fellow with the Advanced Micro and Nanosystems Laboratory, Department of Mechanical and Industrial Engineering, University of Toronto, Toronto, ON, Canada, from 2015 to 2018. He is currently an Assistant Professor with the College of Artificial Intelligence, Nankai University. He is also with the Institute of Intelligence Technology and Robotic Systems, Shenzhen Research Institute of Nankai University, Shenzhen, China. His research interests include automated drug screening, robotic beating heart cell manipulation systems, robotic cell manipulation, and robotic cell measurement.

Mingzhu Sun (Member, IEEE) received the B.S. degree in computer science and technology, the M.S. degree in computer application, and the Ph.D. degree in control theory and control engineering from Nankai University, Tianjin, China, in 2003, 2006, and 2009, respectively.

Since 2009, she has been a Lecturer with the Institute of Robotics and Automatic Information System, Nankai University. She is also with the Institute of Intelligence Technology and Robotic Systems, Shenzhen Research Institute of Nankai University, Shenzhen, China. Her research interests are in micromanipulators, image processing, and computer vision.

Xin Zhao (Member, IEEE) received the B.S. degree in control theory and control engineering from Nankai University, Tianjin, China, in 1991, the M.S. degree in control theory and control engineering from the Shenyang Institute of Automation, CAS, Shenyang, China, in 1994, and the Ph.D. degree in control theory and control engineering from Nankai University, in 1997.

He joined the faculty at Nankai University, in 1997, where he is currently a Professor and the Dean of the College of Artificial Intelligence. He is also with the Institute of Intelligence Technology and Robotic Systems, Shenzhen Research Institute of Nankai University, Shenzhen, China. His research interests are in micromanipulators, microsystems, and mathematical biology.

Yaowei Liu (Member, IEEE) received the B.Eng. degree in automation and the Ph.D. degree in control theory and control engineering from Nankai University, Tianjin, China, in 2013 and 2019, respectively.

He is currently a Post-Doctoral Fellow with the College of Artificial Intelligence, Nankai University. He is also with the Institute of Intelligence Technology and Robotic Systems, Shenzhen Research Institute of Nankai University, Shenzhen, China. His research interests include micromanipulators and microsystems.